

Molecular Modelling of Nanopore Structures

by

Thomas C. McDermott, BE

**Submitted to the School of Chemical and Bioprocess Engineering,
University College Dublin,
for the degree of Doctor of Philosophy (PhD)**

October 2011

Under the supervision of
Prof. J.M.Don MacElroy, BE, PhD, MAIChE, MIChE



An Choláiste Ollscoile, Baile Átha Cliath
Scoil na hInnealtóireachta Ceimicí agus Bithphróisis

where $\text{anint}(A)$ returns the nearest integer to A , and $\text{sign}(A,B)$ returns A with the sign of B are standard Fortran functions. Although these and other forms (Allen and Tildesley (1987)) are equivalent, the speed of compiler implementations can vary considerably, and considering that the PBC calculation of distances and separation vectors usually takes place at the heart of deeply nested force or energy calculation loops, the particular method chosen can have a significant impact on the simulation speed. For this reason it is worthwhile implementing the PBC calculation as a function which compilers can be instructed to inline aggressively (thus removing the function call overhead), and the various forms can then be tested for speed by simply changing the definition of the PBC function.

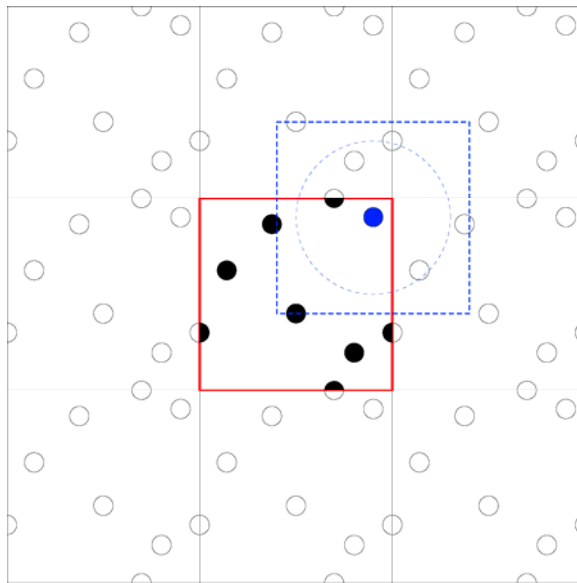


Figure 2.4. Schematic showing periodic boundary conditions in 2D. The dashed blue box illustrates the minimum image condition; the particles in this box, which is centred on the blue particle, are the minimum image neighbours of the blue particle.

the automatic updating of the list, and the selection of the optimum skin thickness, such as those by Thompson (1983) and Chialvo and Debenedetti (1991).

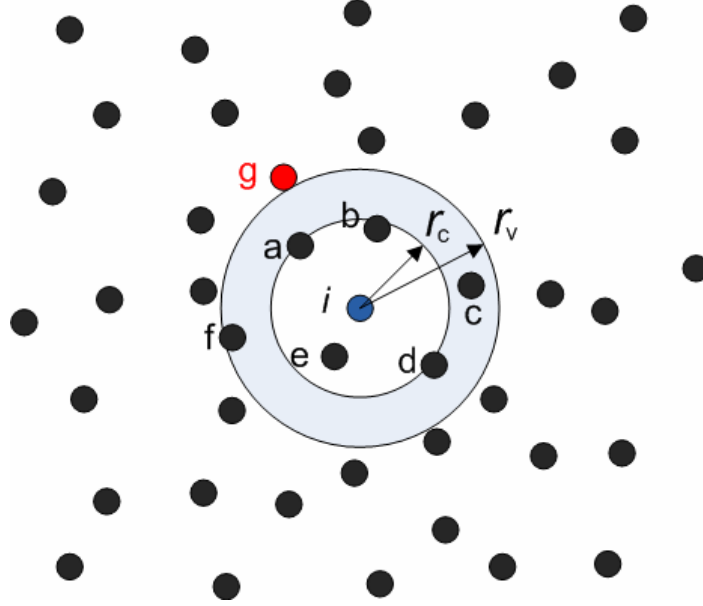


Figure 2.5(a) The Verlet neighbour list for atom i .

The neighbour list may be conveniently stored in two one dimensional arrays as shown in Figure 2.5(b) (a two dimensional array can also be used). The pointer array P stores atom indices for the neighbour list array L , such that $P(i)$ points to the position index in L where the first atom in the neighbour list of atom i is stored, and the last element in the neighbour list for atom i is stored in $P(i+1)-1$, so the neighbours of atom i are stored in the slice $L(P(i):P(i+1)-1)$. For the case where atom i in Figure 2.5(a) is actually $i = 1$, Figure 2.(b) shows the storage in L of the neighbour list includes atoms a, b, c, d, e, f. While looping through the neighbour list to calculate the force on atom $i = 1$, all 6 neighbours are considered, though only those less than r_c (a,b, and e) at a given step actually contribute. For

references, until the last element is reached (which links to zero) as illustrated in Figures 2.6(b) and 2.6(c).

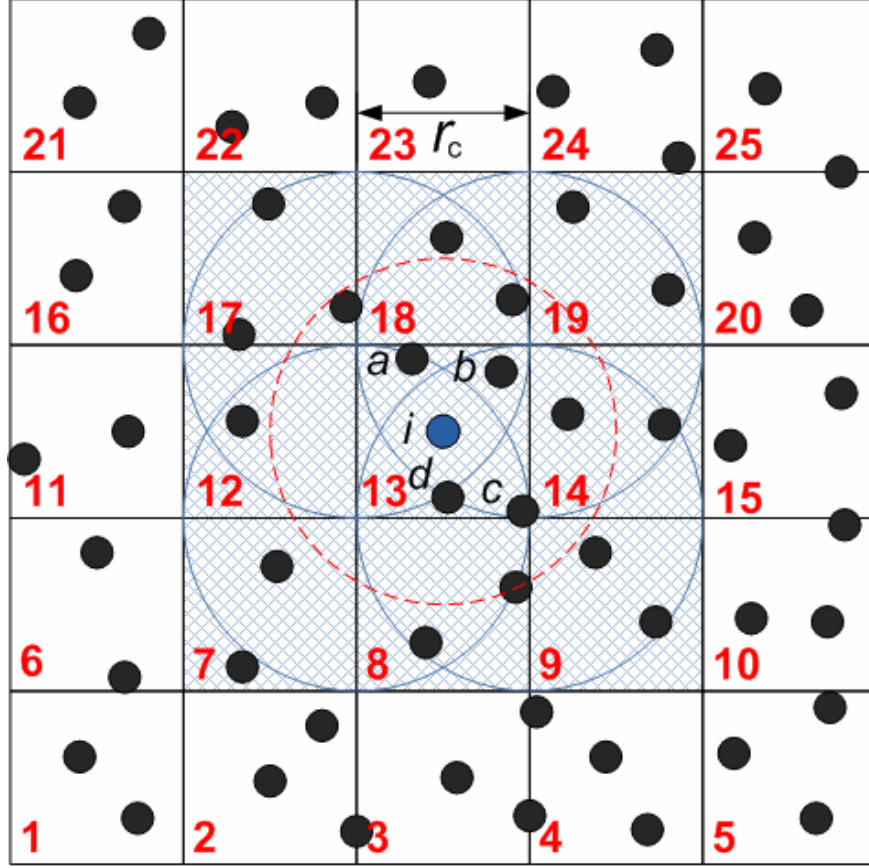


Figure 2.6(a) Two dimensional illustration of the cell list: the simulation box is divided into 25 cells of width r_c such that particle i in a given cell only interacts with particles in the same cell and neighbouring cells. The cell numbers are the red numbers in the bottom left hand corner of each cell. The central cell number 13, contains atoms i , a , b , c , and d , where atom number $i > d > c > b > a$ so that when the list of atoms in the cell is constructed i is added last and is thus the number of the pointer ($HOC(13) = i$) into the list of atoms in the cell as shown in figure 2.6(b).

As in the case of the Verlet list, for molecular dynamics it is possible to traverse both the cells and the linked lists within them in such a way that interaction ij need only be calculated once (Allen and Tildesley (1987)). As noted above, the cell list method may be combined with the Verlet list to improve performance – Frenkel and Smith (2002) provide further analysis of the relative speeds, of the Verlet list, cell list, and a combination of the two for various numbers of Lennard-Jones particles.

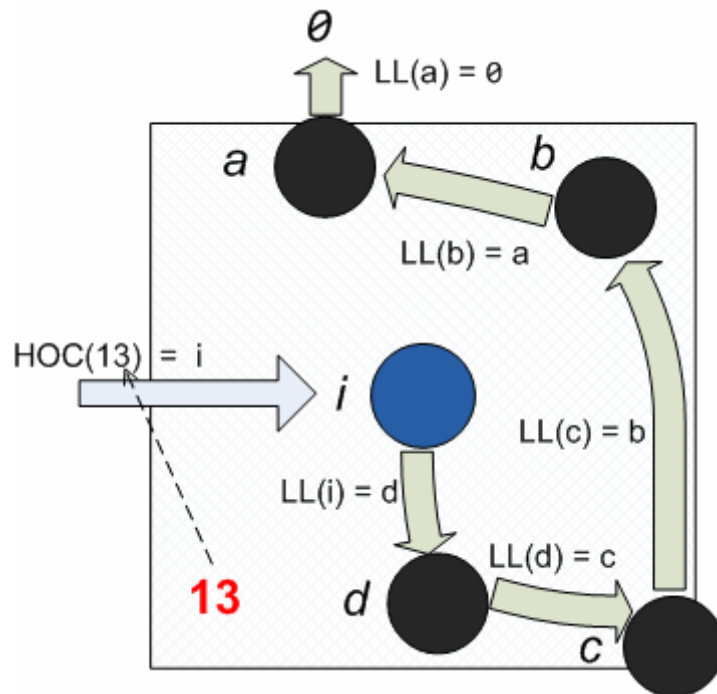


Figure 2.6(b) Linked list chain of atoms in cell. The storage of the list of atoms in cell 13 of figure 2.6 (a) is illustrated. HOC , the “head of the chain” for cell 13 points to atom i . The remaining atoms are then found by following the linked list LL for the remaining atoms in the cell, until the terminating atom (which points to zero) is reached.

2.4.3.7 Non-Lattice Hoshen-Kopelman Algorithm

Al-Futaisi and Patzek (2003) developed a generalization of the original HK algorithm to non-lattice environments which can be used for continuum systems or disordered networks. By using general data structures for describing the network connectivity (which are presented below) the algorithm can handle any arbitrarily connected bonds and sites on any lattice or non-lattice environment of any dimensionality.

The algorithm is illustrated by showing the result of its application to a simple network of 16 nodes and 24 links as given by Al-Futaisi and Patzek (2003) and shown in Figure 2.7(a) below.

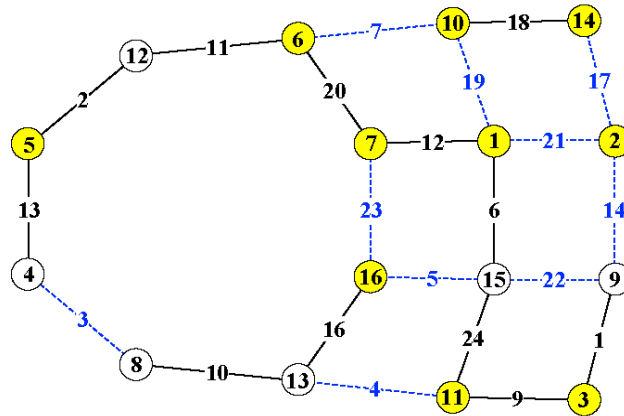


Figure 2.7(a). Simple network of 16 nodes and 24 links (redrawn from Fig. 1 of Al-Futaisi and Patzek (2003)). The yellow disks and full black lines represent occupied nodes and links respectively, while the white disks and dashed blue lines represent empty nodes and links. Each disk/line is labelled with its node/link number.

Cluster	Nodes	Links
1	1, 6, 7	6, 11, 12, 20
2	2	
3	3, 11	1, 9, 24
4	5	2, 13
5	10, 14	18
6	16	16
7		10

Table 2.2 Cluster labels for nodes and links as shown in Figure 2.7(b) for the network shown in Figure 2.7(a)

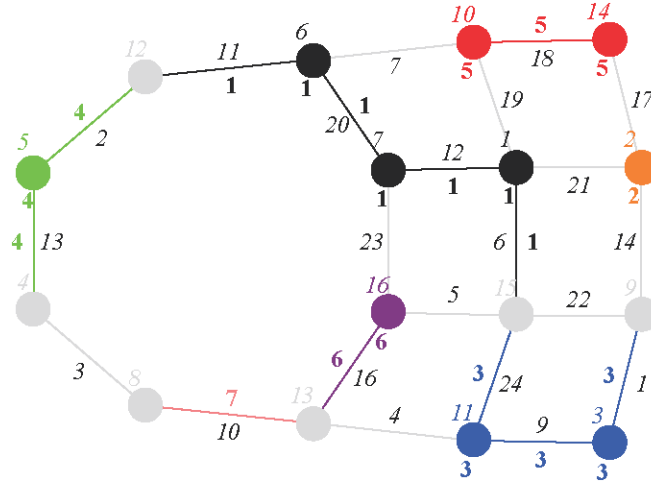


Figure 2.7(b). The labels which have been assigned to the network by the non-lattice Hoshen-Kopelman algorithm. Each occupied node and link is given a unique colour depending on the cluster it belongs to. The **bold** coloured labels give the cluster numbers of the nodes and links while the *italic* labels are the node/link numbers. The light grey elements are empty (nodes or links) and so have no cluster numbers.

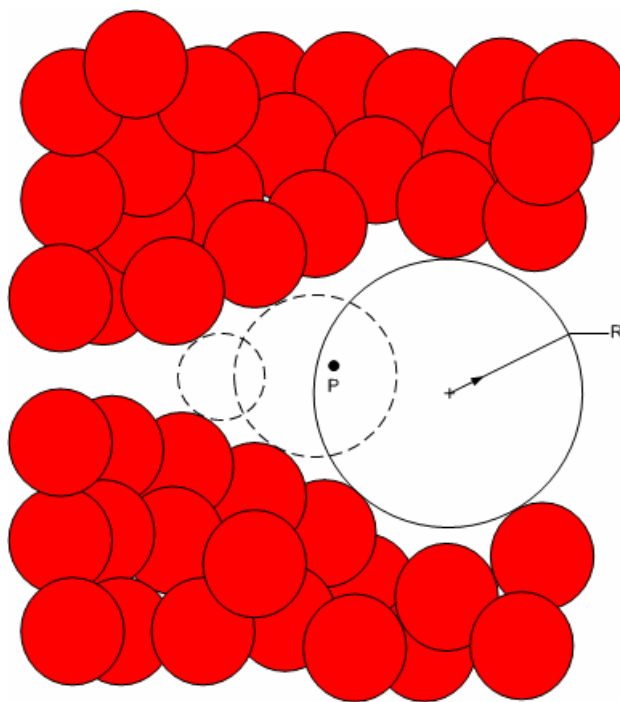
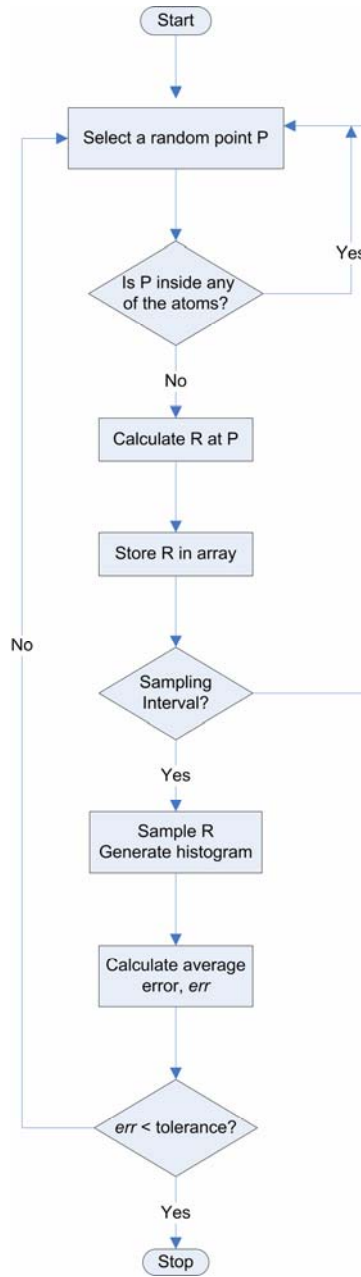
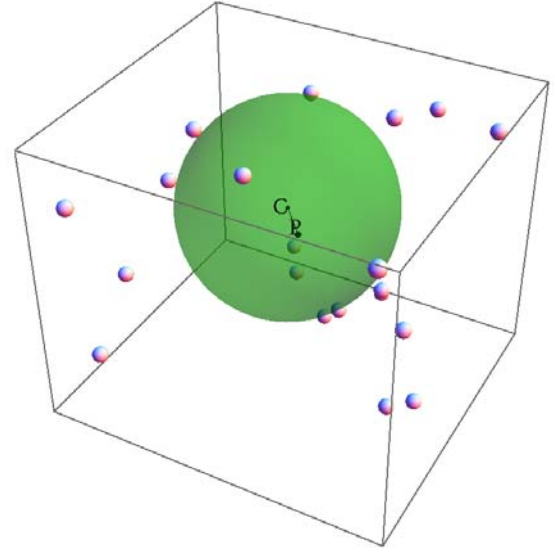


Figure 2.8. Definition of the pore size used by Bhattacharya and Gubbins (2006). The pore wall atoms are the red disks. The circle shown with radius R represents the largest sphere covering point P in the pore.

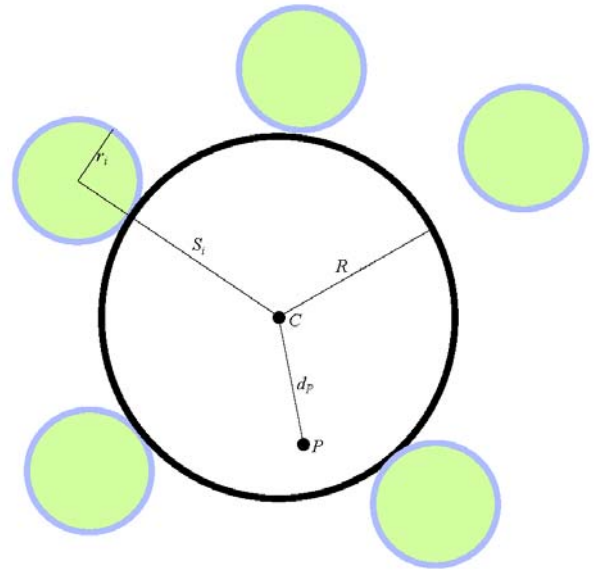
The pore volume function $V(r)$ may be determined by a Monte Carlo volume integration (Allen and Tildesley (1987)) as used by Gelb and Gubbins (1999) where the calculated geometric pore size distributions for models of porous Vycor glass were compared with pore size distributions extracted from simulated adsorption isotherms in order to determine how the geometric definition could be related to the experimental pore size distributions determined from adsorption isotherms. The adsorption isotherms were generated using the Grand Canonical Monte Carlo procedure (Norman and Filinov (1969), Adams (1975), Nicholson and Parsonage (1982) and Frenkel and Smit (2002)) and the pore size distributions were extracted from the isotherms using a slightly modified form of the Barrett-



(a)



(b)



(c)

Figure 2.9. (a) Flowchart for the PSD calculation. (b) The green sphere is centred at C and is the largest sphere covering point P which does not intersect the atoms. (c) A 2D representation of the system shown in (b), C is the largest circle, radius R , containing point P but not intersecting any of the disks (atoms) of radius r_i . The distance from C to the centre or atom i is s_i and from C to P is d_p .

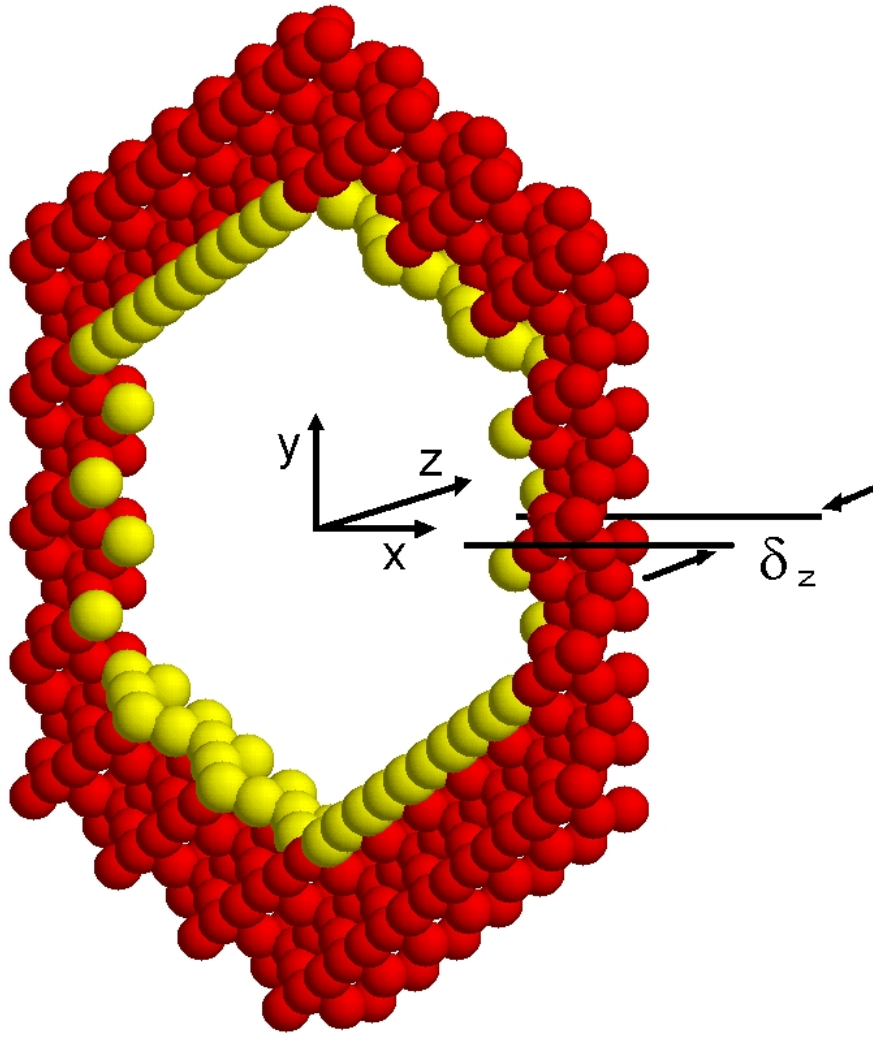


Figure 3.1(a) Single lattice unit of the crystalline structure of the pore wall

The etching process entails the removal of all silicon and oxygen atoms within the x-y boundaries indicated in Figure 3.1(a) and during this process the oxygen atoms within the remaining solid structure are either doubly bonded (siloxane linkages) or singly bonded to the substrate silicon atoms. The doubly bonded oxygens are depicted as red in the figure and the singly bonded oxygens are shown as yellow. In the simulations the latter are treated as united atom hydroxyl groups.

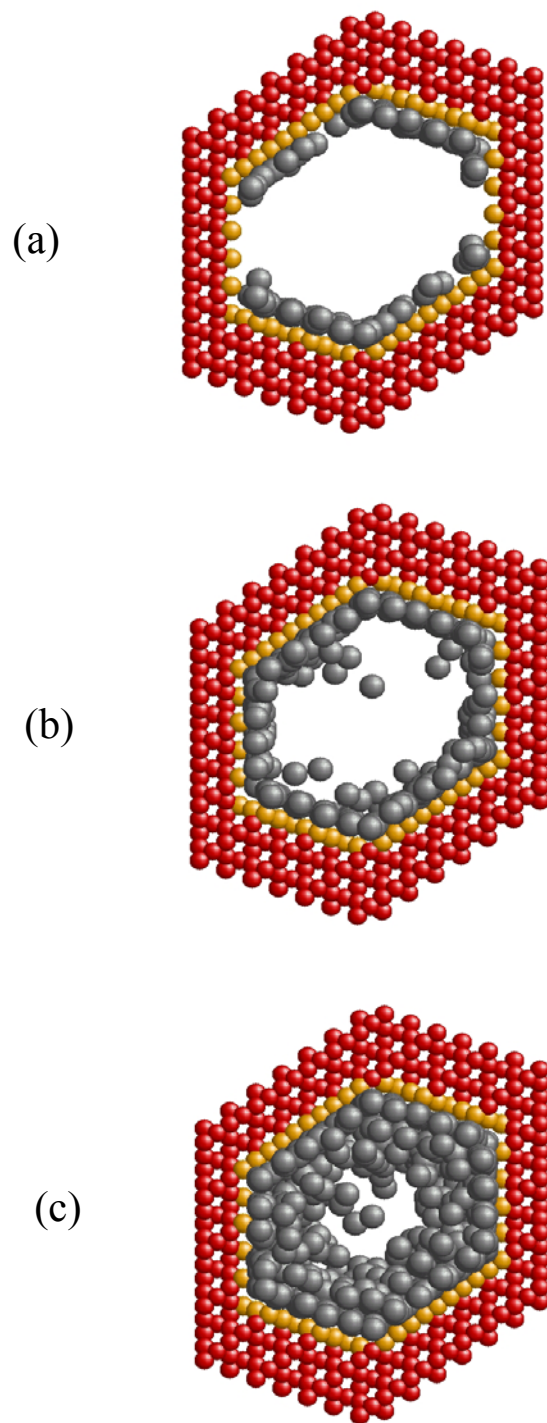


Figure 3.4. Snapshots of the formation of the adsorbed layer within the crystalline silica pore under capillary supercritical conditions ($T = 130\text{K}$). These results correspond to the three points at $\mu^{\text{ex}}/kT = -13$ (a), -10 (b) and -8 (c) in Figure 3.3.

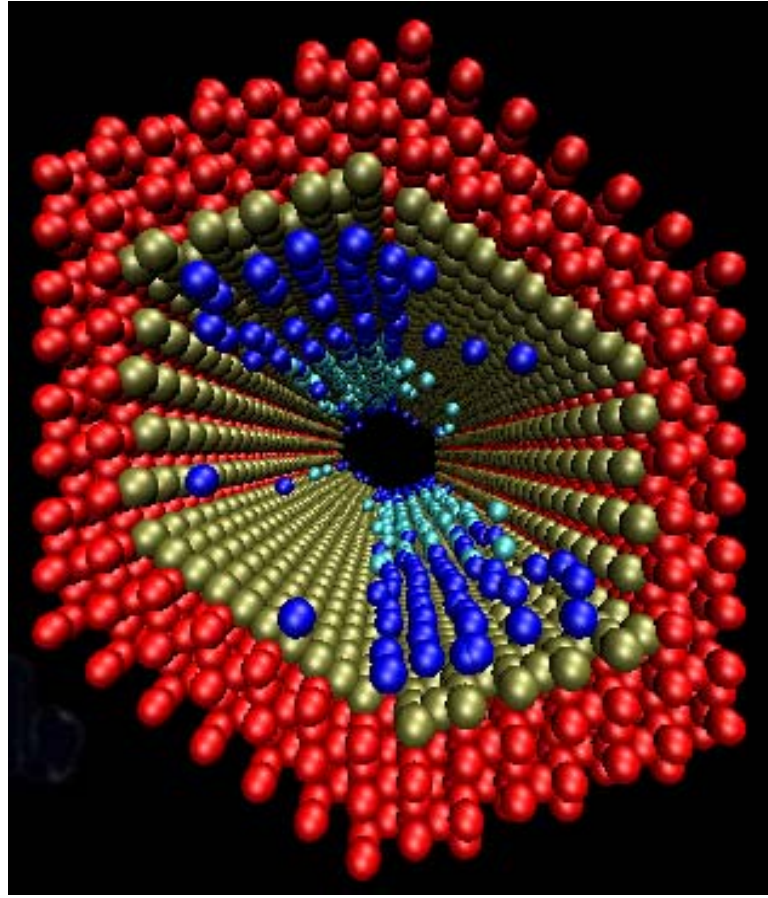


Figure 3.5. View along the pore axis for $\mu^{\text{ex}}/kT = -14$ at 130K.

3.4.2.3 Pozhar-Gubbins Theory

Also shown in Figure 3.6 are the results for the pore averaged self-diffusion coefficient predicted by PG theory. The manner in which these results were obtained differs slightly from the procedure described earlier by MacElroy et al (2001). The expression for the local cross-sectional averaged flux expression provided by PG theory (within the scope of the pseudo-homogeneous approximation discussed in MacElroy et al (2001)) is given by

also serves to emphasise the relative importance of re-collisional events with the static wall particles.

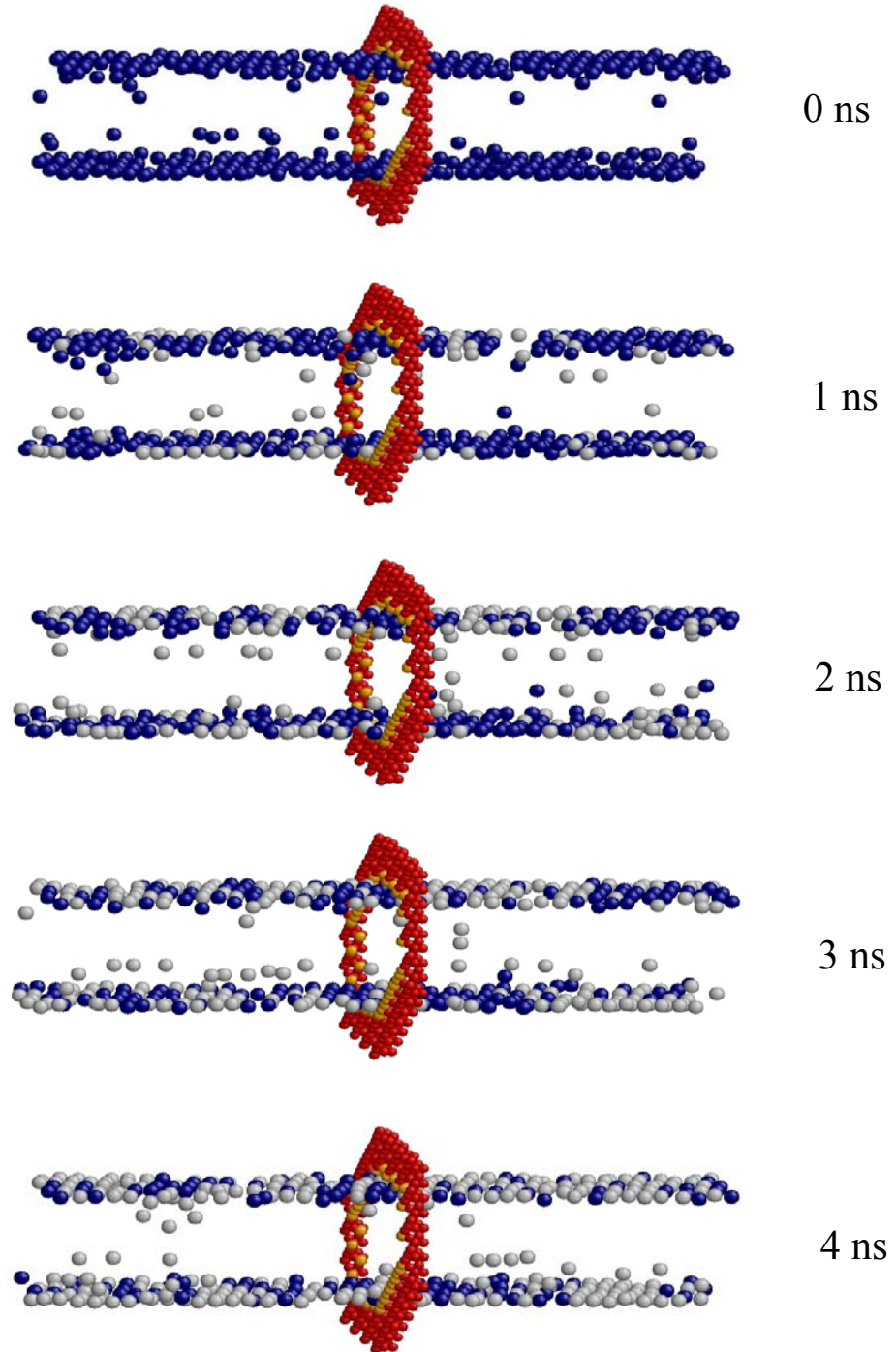


Figure 3.10. Snapshots (taken at times of 0, 1, 2, 3, and 4ns) of the adsorbed particles for the system with the lowest loading at $T = 130\text{K}$. The dark spheres are the particles that have not moved more than 20\AA up until the time corresponding to the frame. Only one solid lattice unit is shown for reference.

of a thin film of silica which has been deposited onto a mesoporous/microporous substrate material (McCann (2010)). The thin 100 nm film shown to the right of the SEM image was fabricated via atmospheric pressure plasma liquid deposition (APPLD) and was reported by McCann (2010) to have an ideal permselectivity for the gases Helium and Nitrogen of $\text{He}/\text{N}_2 = 55$ and an estimated nominal pore size of 0.4 nm.

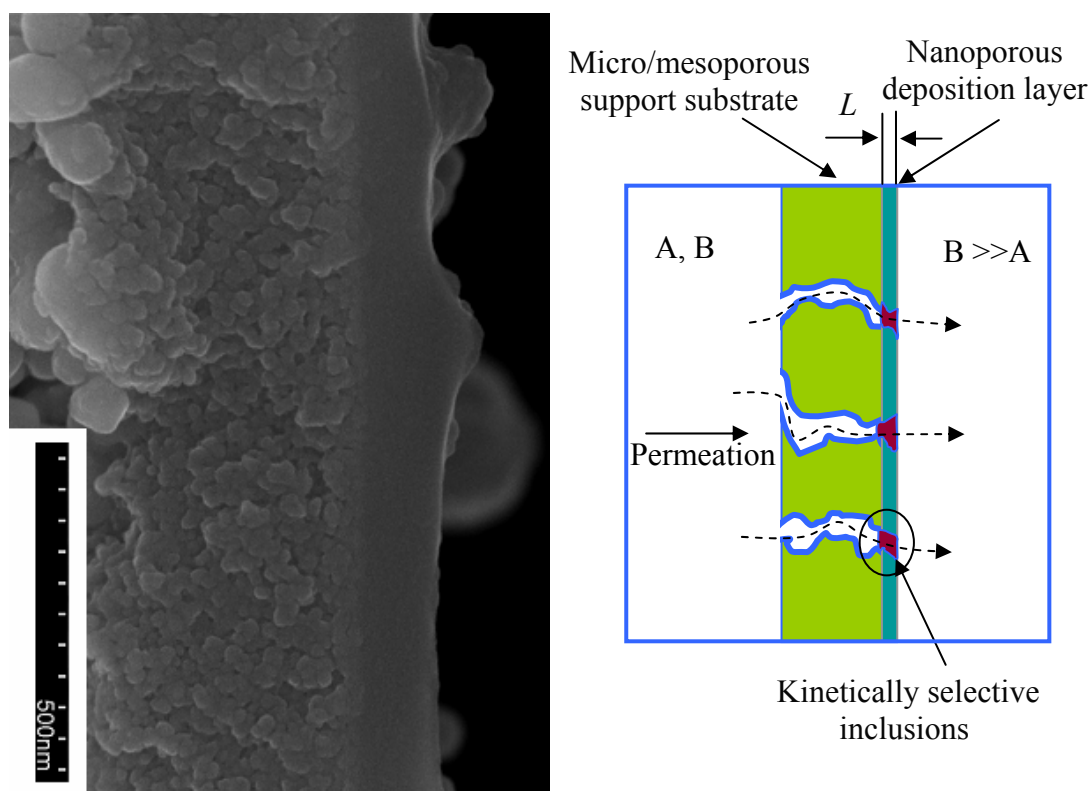


Figure 4.1 (Left) SEM image of a thin film of SiO_2 deposited onto a substrate composed of a secondary 500 nm SiO_2 layer (nominal pore size 1 nm), a microporous γ -alumina (nominal pore size 5-7nm) and a mesoporous α -alumina (nominal pore size in the micron range). The outermost layer on the right of the SEM image is the primary permselective SiO_2 film which is 100 nm in thickness with a nominal pore size of 0.4 nm. (Right) A schematic drawing of the principal elements of a permselective membrane.

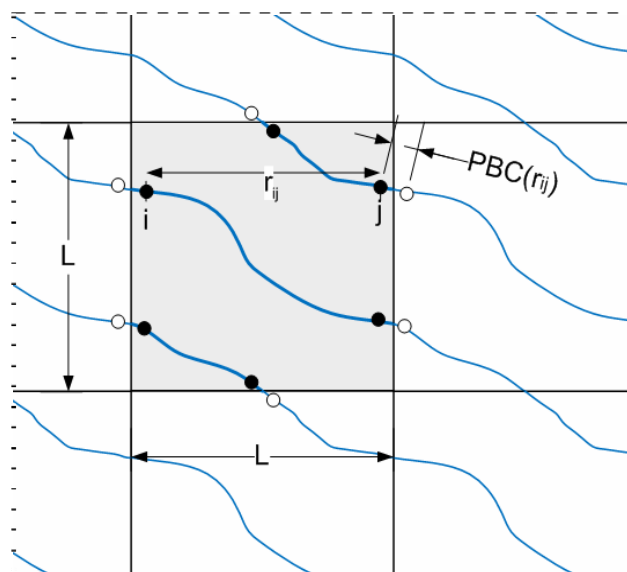


Figure 4.6 A two dimensional representation of the periodic system showing the variables required for determining the bonds which cross the system boundaries. The cluster shown spans both the x and y periodic dimensions, however if the x periodicity is switched off then the resulting two clusters (the top and bottom clusters are joined in the y periodic dimension) do not span the y periodic dimension, but do span the x periodic dimension.

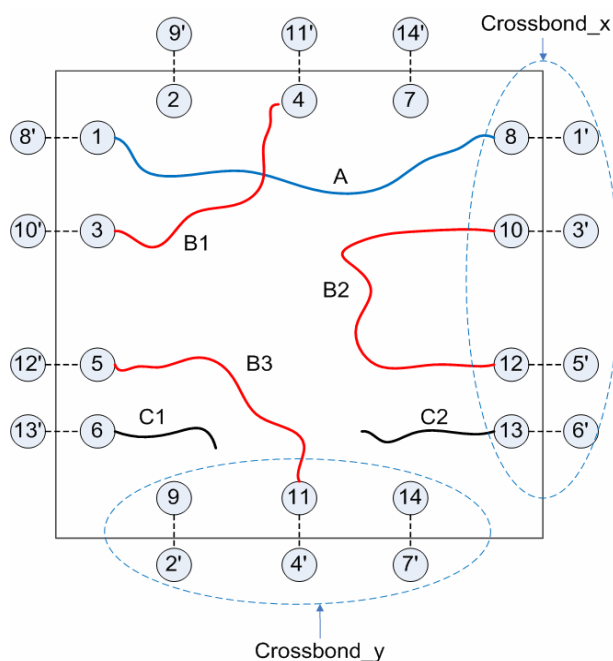
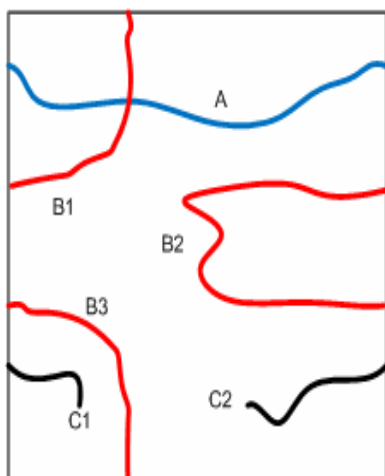
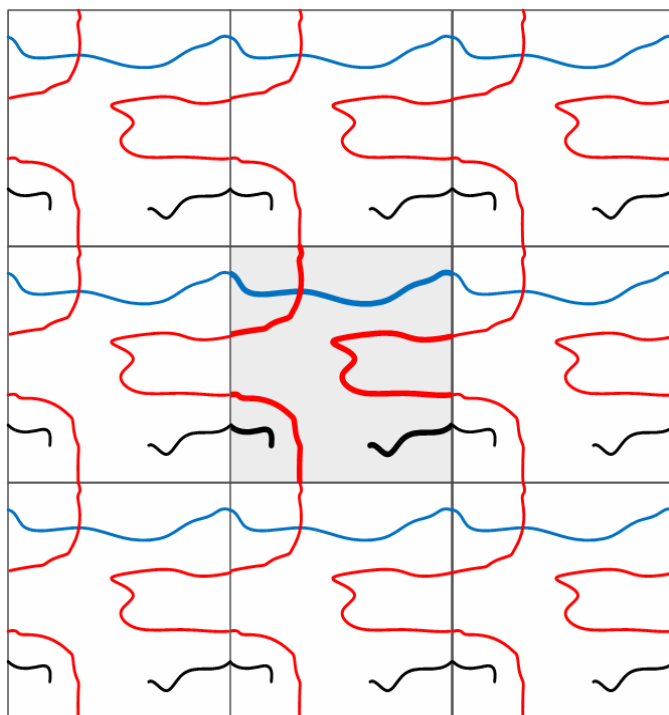


Figure 4.7. Boundary crossing bond in a 2D representation of clusters in a unit cell.



(a) A 2D representation of some molecular clusters in a unit cell with the Periodic Boundary Conditions (PBC) switched off. Note cluster A and B1 are distinct - they are considered to be on different z levels in the actual 3D system.



(b) The unit cell depicted in (a) is highlighted in the central cell which is surrounded by the periodically imaged neighbouring cells.

Figure 4.8. Two dimensional representations of clusters in a periodic system.

When the x-periodicity is switched off then the black segment in part (b) which crosses the x periodic boundary is broken into the two clusters C1 and C2 shown in (a). Removal of the x periodicity also causes the y periodic dimension spanning red segment shown in part (b) to split into the three clusters C1, C2, and C3 which do not span. The cluster marked A spans the x periodic dimension when both the x and y periodicities are switched off.

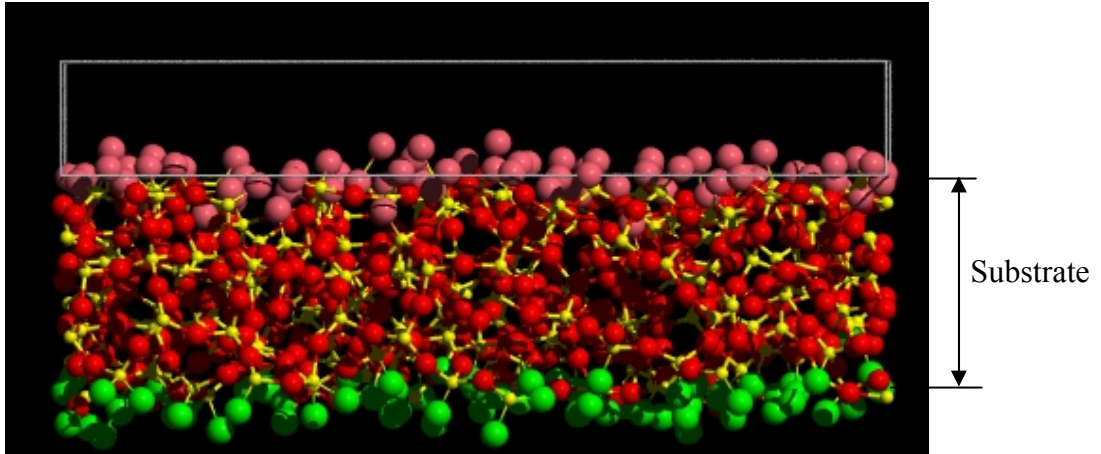


Figure 5.1: A snapshot of the initial amorphous 3.56643nm x 3.56643nm x 1.5nm substrate used for deposition in this model. The green atoms represent the bottom surface and the pink atoms correspond to the top surface hydroxyl groups which serve as reactive seed sites for the deposition process.

In the simulation of the deposition of TEOS the nine irreversible reactions listed in Table 5.1 are considered to take place (Coltrin et al (2000)). Furthermore, in both the $\text{Si}(\text{OH})_4$ and TEOS deposition studies the surface condensation (annihilation) reaction



also takes place.

For simplicity in all of the simulations conducted here only reactions which may be considered to be taking place on the solid surface or within the growing

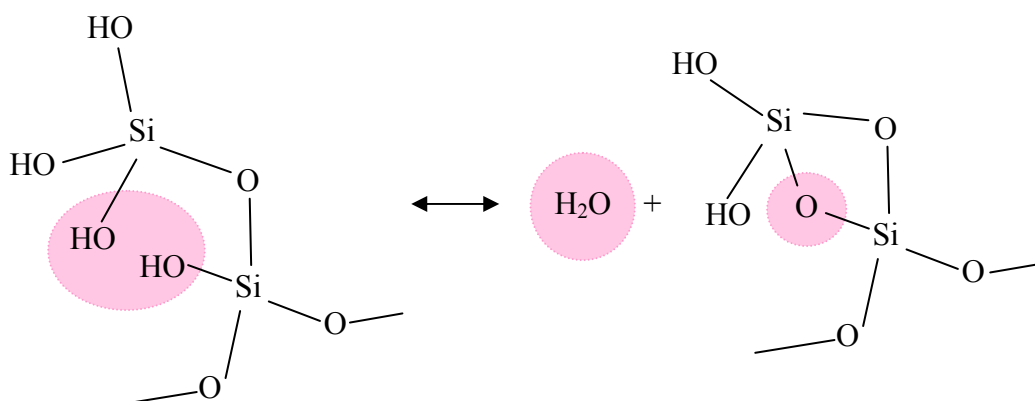


Figure 5.3: The hypothetical formation of a strained two-membered oxygen ring during silanol condensation.

5.3 The Kinetic Monte Carlo Algorithm

5.3.1 The Reaction Frequencies and Reagent Partitioning

The evolution of the silica (SiO_x) film is simulated using the Bortz-Kalos-Lebowitz (1975) lattice kinetic Monte Carlo (KMC) method in conjunction with a hybrid off-lattice relaxation process. In the KMC process the reactive deposition precursor (silicic acid or TEOS) from the vapour phase is incorporated within the growing solid film and transformed into surface sites. The simulation space is discretized into small subcells each of dimension $0.5095 \text{ nm} \times 0.5095 \text{ nm} \times 0.5 \text{ nm}$ ($=\Delta V$) (see Figure 5.4). During the growth process, each subcell of the three dimensional simulation box can be occupied by one or more silicon sites which are bonded to a combination of molecular groups ($-\text{OH}$, $-\text{OCH}_2\text{OCH}_3$ or bridging oxygens) and the occurrence of one of the reactions at one of the sites is termed an event. At each KMC step the frequency of each reaction event in each subcell is calculated and the choice of reaction event, r , to be undertaken is determined by the

probability P_r which is proportional to the frequency of the associated surface reaction relative to the sum of all such frequencies.

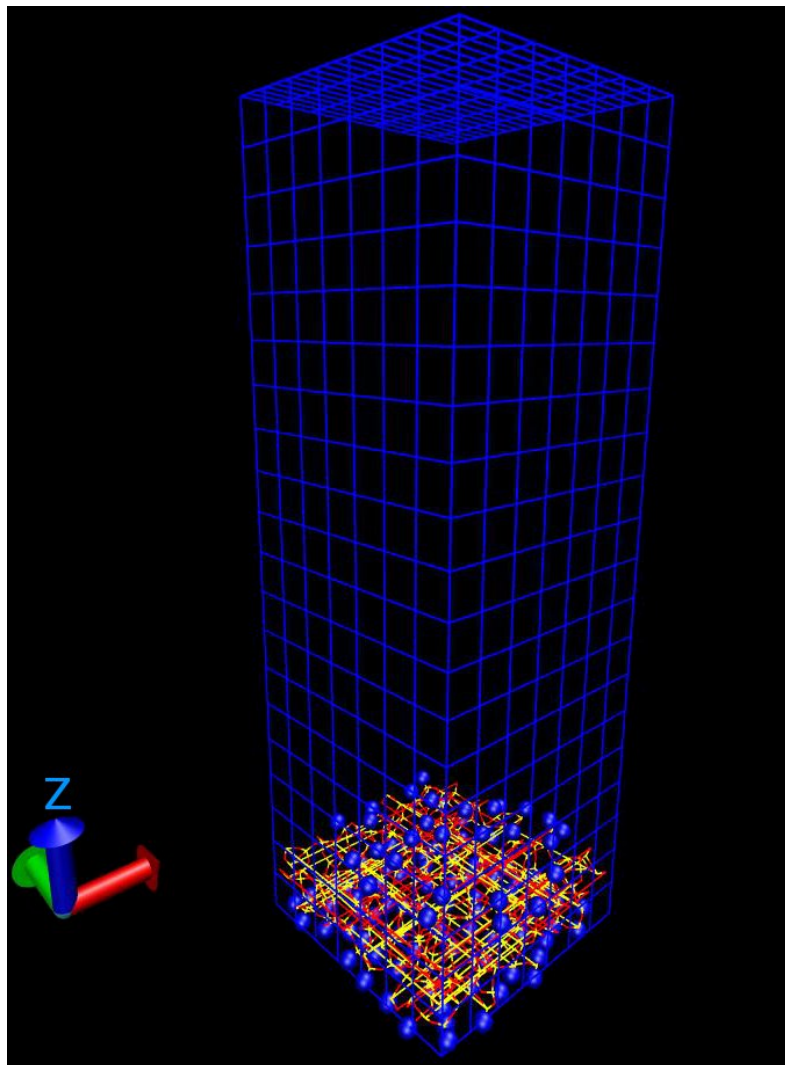


Figure 5.4 The grid of subcells employed in the KMC deposition algorithm.

The frequencies of the reactions are provided by the instantaneous conservation equation of the reacting species as defined locally in time and space by the expression

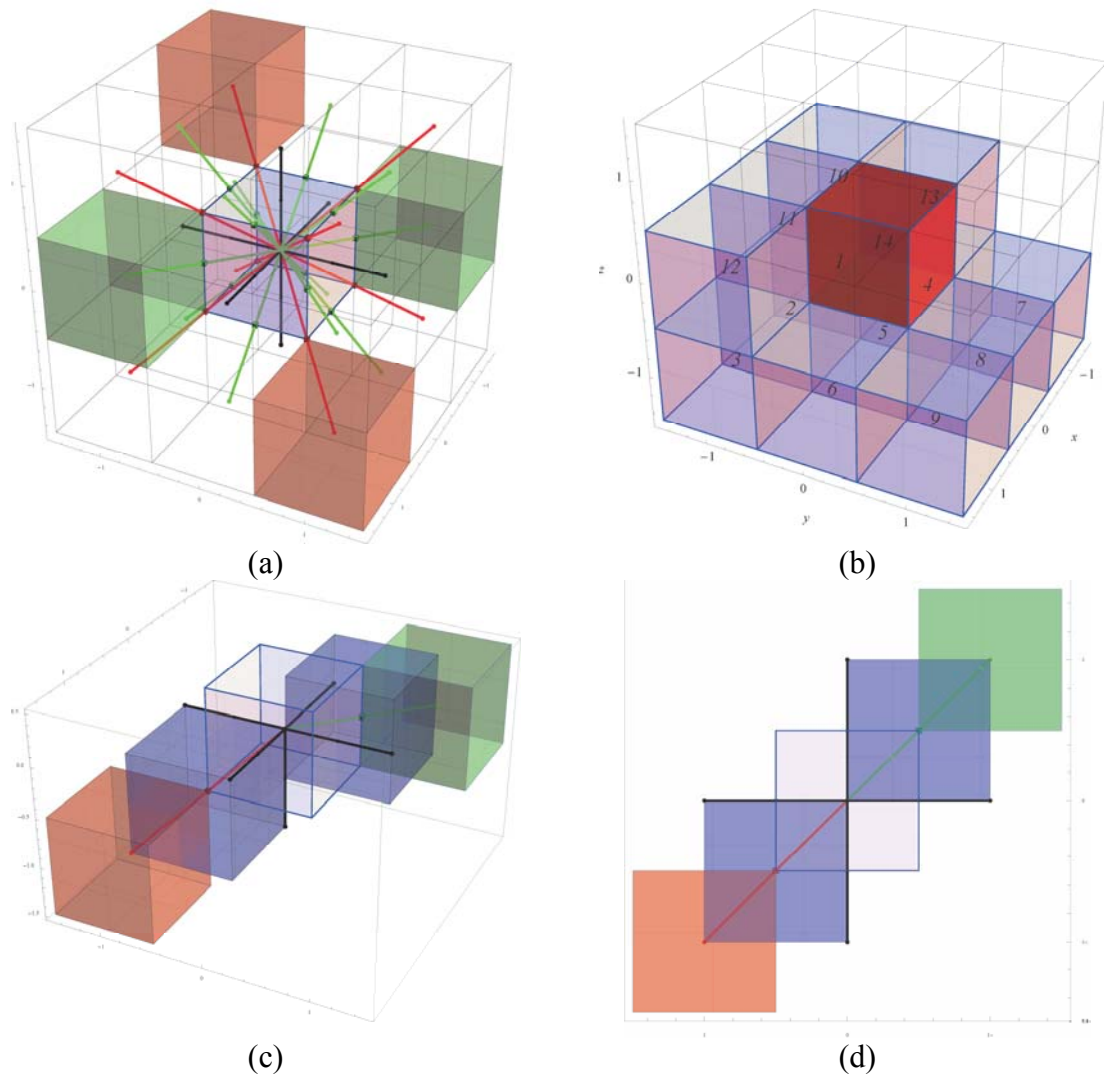


Figure 5.5. Cell connectivity on the 3D lattice. (a) A cell with its 27 neighbours is shown with two edge sharing neighbours and two corner sharing neighbours highlighted. The lines show the possible links between the cell nodes for the case where the full non-lattice version of the Hoshen-Kopelman algorithm is used. (b) The central cell (cell number 14) and its 13 previously examined neighbours. (c) A cell with one corner sharing neighbor (orange cell in bottom left hand corner) and one edge sharing neighbor shown (green cell in top right hand corner). The blue cells centered on the links between the central cell and these neighbours are the regions for determining whether these links are considered occupied or empty (blocked). (d) Top down view of (c)

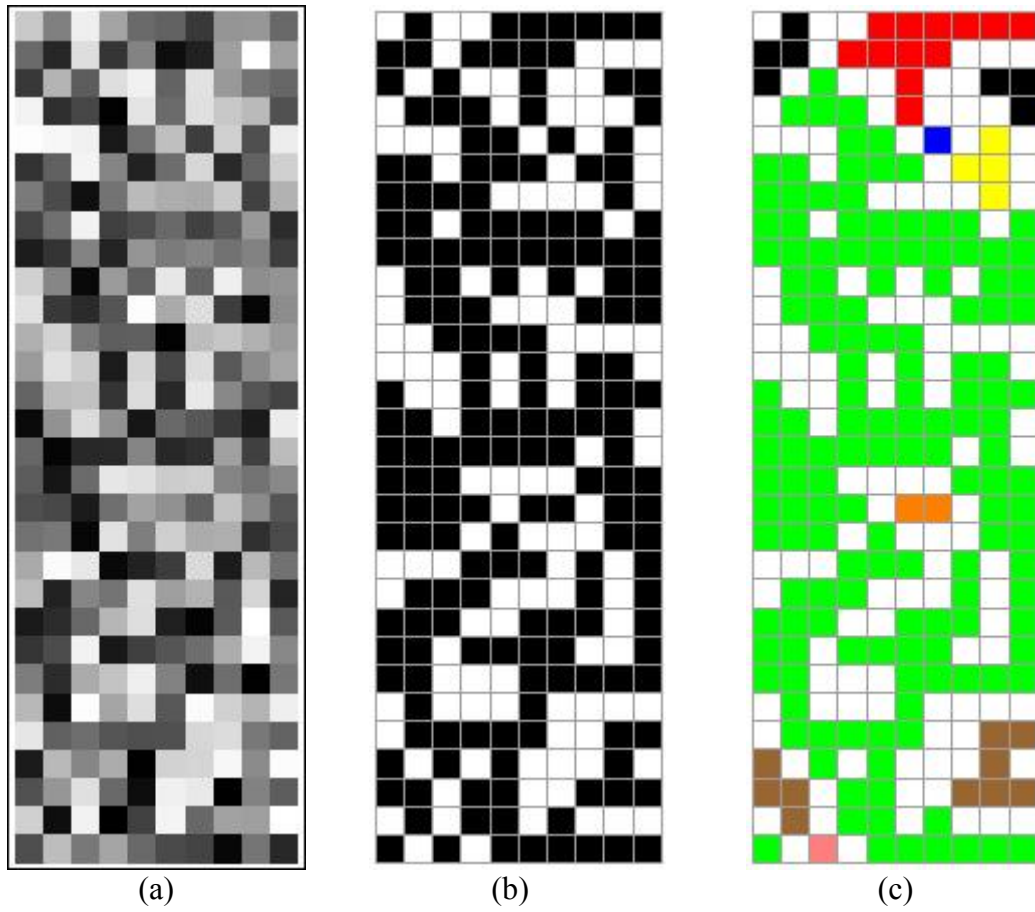


Figure 5.6. Two-dimensional example of the deposited layer (each layer divided into 0.5 nm squares). (a) An initial mapping of the relative magnitudes of the partition coefficients, (b) mapping of those subcells with $K < 0.03$ (white) and those with $K > 0.03$ (black), (c) cluster structure as determined by the Hoshen-Kopelman algorithm.

In general one may select the connectivity between clusters such as those shown in Figure 5.6(c) as appropriate to the given situation. In the studies reported in this work ‘coloured’ cells adjoining through edges and corners as well as faces are considered to be fully connected and hence the example shown in Figure 5.6 (c) is fully percolating from top to bottom.